Available online at www.sciencedirect.com
ScienceDirect
International Journal of Heat and Mass Transfer 51 (2008) 4287–4299
International Journal of HEAT and MASS TRANSFER
www.elsevier.com/locate/ijhmt

Investigation of soot transport and radiative heat transfer in an ethylene jet diffusion flame

C.B. Saji, C. Balaji *, T. Sundararajan

Department of Mechanical Engineering, Indian Institute of Technology Madras, Chennai 600 036, India

Received 11 July 2007; received in revised form 7 February 2008
Available online 8 April 2008

Abstract

Numerical and experimental investigations highlighting the heat and mass transfer phenomena in a laminar co-flowing jet diffusion flame have been carried out. The fuel under consideration is ethylene, with ambient air as the co-flowing oxidizer. The diffusion flame is modeled using a 17-step reduced reaction mechanism with finite rate chemistry and the effects of soot on the radiative heat transfer of the flame have been demonstrated. Soot growth and oxidation processes are studied using a two-equation transport model, while the radiative heat transfer is modeled using the P1 approximation. An in-house finite volume code has been developed to solve the axi-symmetric Navier–Stokes equations in cylindrical coordinates, along with the soot mass fraction, soot number density, energy and species conservation equations. Comparison of predictions with experimental results shows reasonable agreement with regard to the flame height and temperature distribution. A parametric study is also presented, which illustrates the effects of the fuel jet Reynolds number and the flow rate of co-flow air.

Keywords: Numerical and experimental investigations; Laminar; Co-flow; Ethylene jet diffusion flame; Soot; Radiation

1. Introduction

Soot produced in a flame has both beneficial and detrimental effects. In applications like furnaces, the radiation heat transfer associated with soot particles provides a more uniformly heated environment. On the other hand, the presence of un-oxidized soot particles in any combustion exhaust is viewed as environmental pollution. Soot formation is significant, particularly in the case of unsaturated hydrocarbons with double and triple carbon–carbon bond structure (for example ethylene, acetylene and benzene). The present work investigates the effects of soot formation and oxidation on radiative heat transfer from the flame as well as on the overall combustion process, in an ethylene diffusion flame.

Several experimental and numerical studies are available on the modeling of diffusion flames [1–4]. Mitchell et al. [5] studied the laminar diffusion flame of methane in air and predicted the distributions of temperature, velocity and species concentrations. More recently, the application of detailed chemical kinetic models has become an important tool in combustion simulation [6]. Frenklach and co-workers [7] considered about 600 elementary reaction steps and 200 species, including those related to soot chemistry, during acetylene pyrolysis. Such detailed kinetic models, however, are cumbersome to handle due to the large computational times involved. A reduced reaction mechanism for methane combustion has been discussed by Peters and Kee [8]. Various semi-empirical soot models have also been developed, improved and used extensively in laminar diffusion flames [9–12]. Guo et al. [13] have investigated the influence of thermal diffusion on soot formation in an ethylene flame. Ethylene diffusion flame with co-flow air has been studied using a detailed 64-step reaction mechanism by Kennedy et al. [14]. The formation and growth of soot particles in co-annular ethane and ethylene diffusion flames have been studied by Santoro et al. [15],

* Corresponding author. Fax: +91 44 22574652.
E-mail address: balaji@iitm.ac.in (C. Balaji).

0017-9310/$ - see front matter © 2008 Elsevier Ltd. All rights reserved.
doi:10.1016/j.ijheatmasstransfer.2008.02.010

Nomenclature

a	absorption coefficient, m^{-1}
A_s	soot surface area per unit volume, m^{-1}
Ca	soot agglomeration rate constant
C_{min}	number of atoms per soot particle
C_P	specific heat, kJ/kg K
d	diameter, m
D	mass diffusivity, m^2/s
E_a	activation energy, kJ/kmol
Fr	Froude number ($u_j/g^{0.5}d_j^{0.5}$)
g	acceleration due to gravity, 9.81 m/s^2
h	specific enthalpy, kJ/kg K
k	thermal conductivity, W/m K; also, rate constant of a reaction
K	Boltzmann constant, J/K
L	length of flame, m
M	molar mass, kg/kmol
N	number density of soot
N_A	Avogadro's number, particles/kmol
p	pressure, N/m^2
Pr	Prandtl number (υ/α)
q	heat flux (W/m^2)
r	radial coordinate, m; also, reaction rate.
Re	Reynolds number ($\rho u_j d_j/\mu$)
R_u	universal gas constant
Sc	Schmidt number (υ/D)
S_m, S_n	source terms for soot mass and number density
t	time, s
T	temperature, K
u, v	axial and radial velocity components, m/s
Y	mass fraction
z	axial coordinate measured from jet exit, m

Subscripts and superscripts

i	species i
j	fuel jet inlet conditions
m, mix	corresponding to gaseous mixture
ref	reference quantities at free stream conditions
R	radiation
s	soot
(S)	solid state
T	thermophoretic
*	dimensional quantities

Greek symbols

ρ	density, kg/m^3
μ	coefficient of viscosity, N s/m^2
$\dot{\omega}$	mass based reaction rate , kg/m^3 s; mass rate of production
θ	angular coordinate
σ,τ	normal and shear stress fields, N/m^2

using laser extinction/scattering technique for particle size measurement.

Although a large number of studies have been carried out on diffusion flames and several soot models have been developed recently, there is still a strong need to develop a coupled soot model including radiative heat transfer effects, for the analysis of unsaturated hydrocarbon combustion. It is also desirable to arrive at suitable reduced kinetic mechanisms that provide accurate predictions of the overall combustion process, while being computationally very economical. Such reduced chemistry models will be useful for conducting detailed parametric studies and for highlighting the effects of important process parameters, in practical combustion problems. With these objectives in mind, an axi-symmetric diffusion flame of ethylene with co-flow air has been studied experimentally and numerically in the present work. The numerical predictions have been validated with experimental measurements at different fuel jet Reynolds numbers and mass flow rates of co-flow air.

2. Mathematical formulation

The physical configuration of an ethylene jet diffusion flame with co-flow air is shown in Fig. 1. Ethylene gas is injected vertically through a central pipe and the co-flowing air stream enters through the annular area surrounding the fuel pipe. In the numerical model of the present study, the flow is assumed to be axi-symmetric and laminar. An ideal gas mixture formulation is used to account for the variations in density and other physical/transport properties, with temperature and concentration. Second order phenomena like Soret and Dufour effects have been neglected.

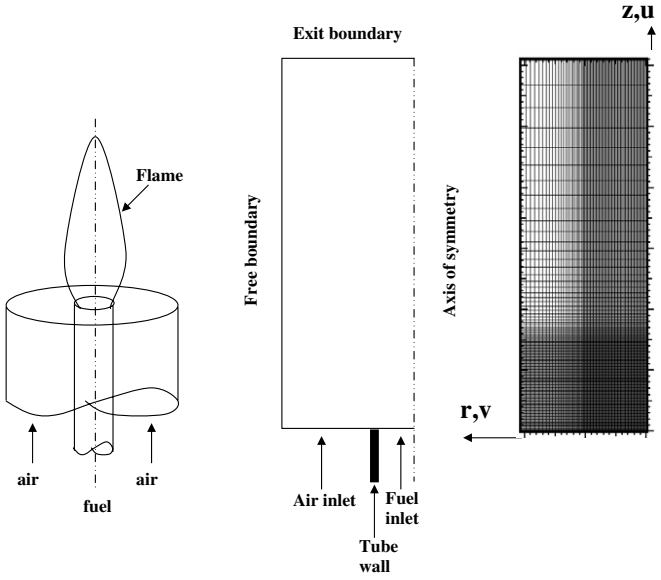

Fig. 1. Geometry of the problem along with the computational domain and grid pattern.

The buoyancy term is included in the momentum equation for z-direction, because of the vertical jet configuration and the low velocity flow considered in the study. Thermophoretic velocities of soot in both r- and z-directions are accounted for, to accurately capture the interactions between the soot and the gas phase flow.

2.1. Governing equations

The governing equations for mass, momentum, energy and species balance are non-dimensionalized using appropriate length, velocity and time scales. The fuel jet inlet velocity (u_j) is chosen as the reference velocity. The diameter of the fuel jet (d_j) is used as the reference length and the ratio of the fuel jet diameter to fuel-jet inlet velocity (d_j/u_j) is used as the time scale. Properties in general, have been normalized using their values at a suitable reference temperature and mixture composition. All the other variables (including the reaction rate $\dot{\omega}_i$), have been non-dimensionalized by combining these reference quantities appropriately. The dimensionless variables are

$$z=\frac{z^*}{d_j},\quad r=\frac{r^*}{d_j},\quad t=\frac{t^*u_j}{d_j},\quad u=\frac{u^*}{u_j},\quad v=\frac{v^*}{u_j},$$
$$\rho=\frac{\rho^*}{\rho_j},\quad p=\frac{p^*}{\rho_j u_j^2},\quad T=\frac{T^*-T_j}{T_j},\quad h=\frac{h^*}{C_{P_{\mathrm{ref}}}T_j}$$
$$\mu=\frac{\mu^*}{\mu_{\mathrm{ref}}}\frac{\mu_{\mathrm{ref}}}{\rho_j u_j d_j}=\frac{\mu^*}{\mu_{\mathrm{ref}}}\frac{1}{Re_j},\quad C_P=\frac{C_P^*}{C_{P_{\mathrm{ref}}}},$$
$$D_{i\mathrm{m}}=\frac{D_{i\mathrm{m}}^*}{D_{\mathrm{ref}}}\frac{D_{\mathrm{ref}}\nu_{\mathrm{ref}}}{\nu_{\mathrm{ref}}u_j d_j}=\frac{D_{i\mathrm{m}}^*}{D_{\mathrm{ref}}}\frac{1}{Re_j Sc_j}$$
$$k=\frac{k^*}{k_{\mathrm{ref}}}\frac{k_{\mathrm{ref}}}{\rho_j u_j C_{P_{\mathrm{ref}}} d_j}=\frac{k^*}{k_{\mathrm{ref}}}\frac{1}{Re_j Pr_j},\quad \dot{\omega}_i=\frac{\dot{\omega}_i^* d_j}{\rho_j u_j}.$$

The dimensionless governing equations in cylindrical polar coordinates (r,z) are given below.

Continuity equation:

$$\frac{\partial\rho}{\partial t}+\frac{\partial}{\partial z}(\rho u)+\frac{1}{r}\frac{\partial}{\partial r}(\rho v r)=0, \tag{1}$$

z-momentum equation:

$$\frac{\partial}{\partial t}(\rho u)+\frac{\partial}{\partial z}(\rho u^2)+\frac{1}{r}\frac{\partial}{\partial r}(r\rho uv)=\frac{\partial}{\partial z}(\sigma_{zz})+\frac{1}{r}\frac{\partial}{\partial r}(r\tau_{zr})+\frac{1}{Fr^2}(\rho_\infty-\rho), \tag{2}$$

r-momentum equation:

$$\frac{\partial}{\partial t}(\rho v)+\frac{\partial}{\partial z}(\rho uv)+\frac{1}{r}\frac{\partial}{\partial r}(r\rho v^2)=\frac{\partial}{\partial z}(\tau_{zr})+\frac{1}{r}\frac{\partial}{\partial r}(r\sigma_{rr})-\frac{\sigma_{\theta\theta}}{r}. \tag{3}$$

The stress terms in the above equations can be written as

$$\sigma_{zz}=-p+2\mu\frac{\partial u}{\partial z},\quad \sigma_{rr}=-p+2\mu\frac{\partial v}{\partial r},$$
$$\sigma_{\theta\theta}=-p+2\mu\frac{v}{r},\quad \tau_{rz}=\tau_{zr}=\mu\left(\frac{\partial u}{\partial r}+\frac{\partial v}{\partial z}\right).$$

The last term in the z-momentum equation arises from buoyancy effects. The species conservation equation for a particular species "i" is given by

$$\frac{\partial}{\partial t}(\rho Y_i)+\frac{\partial}{\partial z}(\rho u Y_i)+\frac{1}{r}\frac{\partial}{\partial r}(r\rho v Y_i)=\frac{\partial}{\partial z}\left(\rho D_{i\mathrm{m}}\frac{\partial Y_i}{\partial z}\right)+\frac{1}{r}\frac{\partial}{\partial r}\left(r\rho D_{i\mathrm{m}}\frac{\partial Y_i}{\partial r}\right)+\dot{\omega}_i, \tag{4}$$

where $\dot{\omega}_i$ denotes the mass rate of production of species i per unit volume. The energy conservation equation may be written as

$$\frac{\partial}{\partial t}(\rho C_P T)+\frac{\partial}{\partial z}(\rho u C_P T)+\frac{1}{r}\frac{\partial}{\partial r}(r\rho v C_P T)=\frac{\partial}{\partial z}\left(k\frac{\partial T}{\partial z}\right)+\frac{1}{r}\frac{\partial}{\partial r}\left(rk\frac{\partial T}{\partial r}\right)-\sum_{i=1}^{n}\dot{\omega}_i\Delta h_{fi}+\sum_{i=1}^{n}\frac{\partial}{\partial z}\left(\rho D_{i\mathrm{m}}C_{Pi}T\frac{\partial Y_i}{\partial z}\right)+\frac{1}{r}\frac{\partial}{\partial r}\left(r\rho D_{i\mathrm{m}}C_{Pi}T\frac{\partial Y_i}{\partial r}\right)+\nabla\cdot q_{\mathrm{R}} \tag{5}$$

with h_{fi} representing the enthalpy of formation for the ith species and q_{R} denoting the radiative flux. Thermo-physical properties have been evaluated using the Chapman–Enskog description of ideal gas mixtures [16]. The relations used for the evaluation of each of these properties are given in the Appendix.

The divergence of the radiative heat flux term included in the energy Eq. (5) is obtained from the radiation model using "P1" approximation, which belongs to the more general " Pn" model expansion of the radiative transfer equation into an orthogonal series of spherical harmonics. For the sooty flames studied here, radiation transport is better described by assuming the medium to have moderate to large optical thickness, and so the use of P1 approximation is justified [17]. The expression for the heat source (or sink) due to radiation using this approximation is given by [18]

$$-\nabla\cdot q_{\mathrm{R}}=aG-4a\sigma T^4, \tag{6}$$

where 'a' is the absorption coefficient and G is the incident radiation. The transport equation for incident radiation used in the model is given by

$$\nabla\cdot\left(\frac{1}{3a}\nabla G\right)-aG+4a\sigma T^4=0. \tag{7}$$

The value of $-\nabla\cdot q_{\mathrm{R}}$ can be directly substituted to the energy equation to account for radiation. A detailed treatment of the P1 approximation is available in [18].

Emissivities of CO_2 and H_2O are obtained as functions of temperature and pressure including the effect for band overlap, using the modified Hottel's correlations proposed by Leckner [3]. Accordingly, the emissivity at zero partial pressure (for water vapor or carbon dioxide) is given by

$$\varepsilon_{0,\mathrm{S}}=\exp\left[\sum_{i=0}^{M}\sum_{j=0}^{N}C_{ji}\left(\frac{T_{\mathrm{g}}}{T_0}\right)^j\left(\log_{10}\frac{P_{\mathrm{a}}L}{(P_{\mathrm{a}}L)_0}\right)^i\right], \tag{8}$$

Table 1
Correlation constants for the determination of the emissivity of water vapour

$C_{00}C_{10}C_{20}$	−2.2118, −1.1987, 0.035596
$C_{01}C_{11}C_{21}$	0.85667, 0.93048, −0.14391
$C_{02}C_{12}C_{22}$	−0.10838, −0.17156, 0.045915
P_E	$(p+2.56p_a/\sqrt{t})/p_b$ for $t=T/T_0$
$(p_aL)_m/(p_aL)_0$	$13.2t^2$
a	2.144 for $t<0.75$
	$1.888-2.053\log_{10}t$ for $t>0.75$
b	$1.10/t^{1.4}$
c	0.5

where $T_0 = 1000$ K and $(P_aL)_0 = 1$ bar cm. Subscript 'S' represents the species (water vapor or carbon dioxide) accordingly. C_{ji} represent the correlation constants for water vapor and carbon dioxide as shown in Tables 1 and 2, respectively. The emissivity at any partial pressure (for water vapor as well as carbon dioxide) is then found from

$$\varepsilon_{p,S} = \varepsilon_{0,S}\left[1-\frac{(a-1)(1-P_E)}{(a+b-1+P_E)}\exp\left(-c\left[\log_{10}\frac{(P_aL)_m}{P_aL}\right]^2\right)\right], \tag{9}$$

where, values of the effective pressure P_E and the correlation parameters a, b, c, and $(P_aL)_m$ for water vapor and carbon dioxide are also given in Tables 1 and 2, respectively. In order to take care of the band overlap between CO_2 and H_2O, a correction factor has been introduced as

$$\Delta\varepsilon = \left[\frac{\xi}{10.7+101\xi}-0.0089\xi^{10.4}\right]\left(\log_{10}\frac{(P_{H_2O}+P_{CO_2})L}{(P_aL)_0}\right)^{2.76}, \tag{10}$$

where, $\xi = \frac{P_{H_2O}}{P_{H_2O}+P_{CO_2}}$.

Table 2
Correlation constants for the determination of the emissivity of carbon dioxide

$C_{00}C_{10}C_{20}C_{30}$	−3.9893, 2.7669, −2.1081, 0.39163
$C_{01}C_{11}C_{21}C_{31}$	1.2710, −1.1090, 1.0195, −0.21897
$C_{02}C_{12}C_{22}$ C_{32}	−0.23678, 0.19731, −0.19544, 0.044644
P_E	$(p+0.28p_a/\sqrt{t})/p_b$ for $t=T/T_0$
$(p_aL)_m/(p_aL)_0$	$0.054t^2$ for $t<0.7$
	$0.225t^2$ for $t>0.7$
a	$1.0+0.1/t^2$
b	0.23
c	1.47

Table 3
Results of the grid independence study

Grid size	T_{max}	% Change of T_{max}
61 × 41	2148.0	–
81 × 61	2040.4	5.01
121 × 81	2014.9	1.25
181 × 121	2010.38	0.23
241 × 181	2007.9	0.114

The net emissivity for CO_2 and H_2O is now calculated as

$$\varepsilon_{CO_2+H_2O} = \varepsilon_{p,CO_2} + \varepsilon_{p,H_2O} - \Delta\varepsilon. \tag{11}$$

The absorption coefficient of soot has been calculated as a function of soot volume fraction and temperature, using the expression developed by Kent and Honnery [19], based on the experimental data for ethylene–air diffusion flames as

$$a_{soot} = 266.0C_1f_{vs}T, \tag{12}$$

where f_{vs} is the soot volume fraction and the constant C_1 is taken as 7.0 for ethylene. The absorption coefficient for the mixture of CO_2 and H_2O is taken as [11]

$$a_{CO_2+H_2O} = 0.1(X_{CO_2}+X_{H_2O}), \tag{13}$$

where X represents the mole fraction. The net absorption coefficient 'a' for the soot and mixture of CO_2 and H_2O is obtained for each cell, as a sum of the individual absorption coefficients [11]. The emissivity of soot and the net gas emissivity are now obtained using the empirical correlation suggested by Yuen and Tien [20] as follows:

$$\varepsilon_{soot} = (1.0-e^{-a_{soot}L}), \tag{14}$$

$$\varepsilon_{net} = (1.0-e^{-a_{soot}L}) + e^{-a_{soot}L}\varepsilon_{CO_2+H_2O}. \tag{15}$$

2.2. Reaction kinetics for ethylene combustion and soot formation

The simplest approximation that leads to any meaningful evaluation of fuel combustion in air is a single step global reaction [21], with two reactants (fuel and oxygen), two products (carbon dioxide and water vapor) and one inert species (nitrogen). However, considering the complexities involved, especially with the combustion of higher and unsaturated hydrocarbons where soot formation is significant, the single step global reaction involving five species becomes inadequate in capturing the physics of the process. Hence, a 17 step reduced mechanism having 16 major species has been identified from published literature [11–15,22], as discussed below. These kinetic steps can be generally classified as fuel break-up mechanisms (R1)–(R5), CO formation and oxidation (R6)–(R9), hydrogen–oxygen reactions and H_2O formation (R10)–(R12), and finally the formation and oxidation of solid carbon (R13)–(R17).

The fuel break-up steps:

$$C_2H_4 + O \rightarrow CHO + CH_3 \tag{R1}$$

$$C_2H_4 + M \rightarrow C_2H_2 + H_2 + M \tag{R2}$$

$$C_2H_4 + H \rightarrow C_2H_3 + H_2 \tag{R3}$$

$$C_2H_3 \rightarrow C_2H_2 + H \tag{R4}$$

$$CH_3 + M \rightarrow CH_2 + H + M \tag{R5}$$

where M is a third body involved in the reaction.

CO formation and oxidation:

$$CH_2 + O_2 \rightarrow CO + OH + H \quad (R6)$$

$$CHO + M \rightarrow CO + H + M \quad (R7)$$

$$CO + OH \rightleftarrows CO_2 + H \quad (R8)$$

$$CO + O_2 \rightleftarrows CO_2 + O \quad (R9)$$

Hydrogen–oxygen reactions:

$$H + O_2 \rightleftarrows O + OH \quad (R10)$$

$$H_2 + OH \rightleftarrows H_2O + H \quad (R11)$$

$$H + OH \rightleftarrows H_2O \quad (R12)$$

Among the above steps, the reaction involving OH radical (R8) is slow and it usually determines the rate of oxidation of CO to CO_2 with considerable release of thermal energy. The rate constants for the kinetic steps (R1)–(R12) have been taken from the Refs. [6,14,21,22].

Finally, solid carbon is formed or consumed through the reactions

$$C_2H_2 \rightarrow 2C_{(S)} + H_2 \quad (R13)$$

$$C_2H_2 + nC_{(S)} \rightarrow (n+2)C_{(S)} + H_2 \quad (R14)$$

$$C_{(S)} + \frac{1}{2}O_2 \rightarrow CO \quad (R15)$$

$$C_{(S)} + OH \rightarrow CO + H \quad (R16)$$

$$C_{(S)} + O \rightarrow CO \quad (R17)$$

Soot formation mechanism through the acetylene route (steps R2 and R4) was considered, based on the assumption that soot formation from hydrocarbon fuels proceeds via the basic steps of nucleation, surface growth, coagulation, and oxidation. Modified versions of the two-equation transport model for soot, originally proposed by Leung et al. [9] and Fairweather et al. [10], have been successfully used for the simulations of ethylene/air diffusion flames [13,23]. These approaches are also adopted for modeling soot in the present study. The conservation equations for soot mass fraction and particle number density are solved along with the species conservation equations. The transport equations for soot are given as

$$\rho v\frac{\partial Y_s}{\partial r} + \rho u\frac{\partial Y_s}{\partial z} = -\frac{1}{r}\frac{\partial}{\partial r}(r\rho V_{T,r}Y_s) - \frac{\partial}{\partial z}(\rho V_{T,z}Y_s) + S_m, \quad (16)$$

$$\rho v\frac{\partial N}{\partial r} + \rho u\frac{\partial N}{\partial z} = -\frac{1}{r}\frac{\partial}{\partial r}(r\rho V_{T,r}N) - \frac{\partial}{\partial z}(\rho V_{T,z}N) + S_n. \quad (17)$$

The thermophoretic velocities of soot are evaluated [14] as

$$V_{T,x_i} = -0.55\frac{\mu}{\rho T}\frac{\partial T}{\partial x_i} \quad \text{for } x_i = r, z.$$

The soot number density, N, is defined as the number of particles per unit mass of mixture. The source term S_m accounts for the nucleation, surface growth and oxidation effects of soot [9,10], while S_n takes care of the combined effect of soot nucleation and agglomeration [10]. These source terms are given as

$$S_m = 2.0r_{13}M_{C(S)} + 2.0r_{14}M_{C(S)} - (r_{15}M_{C(S)}A_s + r_{16}A_s + r_{17}A_s), \quad (18)$$

$$S_n = \frac{2.0}{C_{min}}N_A r_{13} - 2.0C_a\left(\frac{6.0M_{C(S)}}{\pi\rho_{C(S)}}\right)^{1/6} \times \left(\frac{6.0KT}{\rho_{C(S)}}\right)^{\frac{1}{2}}[C_{(S)}]^{1/2}[\rho N]^{11/6}. \quad (19)$$

In the above equations, $M_{C(s)}$ is the molecular weight of solid carbon (=12.011 kg/kmol) and C_{min} is the number of carbon atoms in the incipient carbon particle (~700) as discussed by [23]. For the constant C_a, a typical value of 3 is used in the present study [10].

The rates of soot nucleation and growth given by the reaction steps (R13) and (R14), are taken as

$$r_{13} = k_{13}[C_2H_2], \quad (20)$$

$$r_{14} = k_{14}f(A_s)[C_2H_2], \quad (21)$$

where, $k_{13} = 1.7\exp(-7548.0/T)$ and $k_{14} = 6.0\exp(6038.0/T)$.

It has been assumed that the functional dependence of soot surface growth, $f(A_s)$, on the soot surface area per unit volume is linear [22]. Following the works of [12,13,23–25], the rates of soot oxidation steps (R15)–(R17) are given as

$$r_{15} = 120.0\left[\frac{k_A X_{O_2}\eta}{1 + k_Z X_{O_2}} + k_B X_{O_2}(1-\eta)\right]f_{O_2}, \quad (22)$$

where $\eta = (1 + \frac{k_T}{k_B X_{O_2}})^{-1}$.

Also

$$r_{16} = \phi_{OH}k_{16}T^{-1/2}X_{OH}f_{OH}, \quad (23)$$

$$r_{17} = \phi_O k_{17}T^{-1/2}X_O. \quad (24)$$

In the above expressions, k, X and f denote the reaction rate constant, mole fraction and a temperature dependent correction factor, respectively. The values of the constants ϕ_{OH} and ϕ_O, have been taken as 0.12 and 0.5, respectively [23,25].

2.3. Boundary conditions

The boundary conditions of the problem are shown in Fig. 1. The bottom surface is taken as an inlet boundary, where the density, velocity, and concentration of the incoming species are specified. A parabolic laminar pipe flow velocity profile has been assigned for the fuel stream. The mass fractions of all reactants and products species, except the fuel ($Y_{C_2H_4} = 1$) are specified as zero in the fuel inlet. For the air stream, a boundary layer profile is assumed close to the outer surface of the fuel pipe and a uniform velocity is prescribed outside it. The mass fractions of oxygen and nitrogen corresponding to those of normal

air ($Y_{OX} = 0$ and $Y_{N_2} = 0.77$) are specified in the air inlet. The mass fraction and number density of soot are also specified as zero at both the fuel and air inlets. The right-side boundary is specified as an axis of symmetry, while the left surface is considered as a free boundary. Along the axis of symmetry, zero gradient condition is applied to all variables, except the radial velocity component 'v', which is set as $v = 0$. On the free boundary as well as on the exit boundary, all the solution variables have been extrapolated in the direction normal to the boundary using three point polynomial fits. In addition, the extrapolated solution thus obtained on the boundary has also been locally smoothened by considering all the neighbors of the node. Irradiation from the boundaries is calculated according to the temperature at the boundary, while the surroundings were considered as infinite and cold (no radiation emitted or reflected from the surroundings).

2.4. Solution procedure

The governing equations have been discretized using the finite volume method. A staggered grid has been used in the present formulation, with pressure nodes located at the centroids of cells formed by the velocity nodes. A semi-implicit time marching procedure is used to integrate the z-momentum and r-momentum equations with respect to time, for updating the velocities for an assumed (guess) pressure field. The guess pressure field is corrected depending upon the magnitude of the continuity residue, by solving a Poisson equation of the form

$$\nabla^2 p' = \text{constant}(\nabla \cdot \rho \bar{v}). \tag{25}$$

The cell pressures are then updated by adding the pressure correction p' at each pressure node, followed by the solution of the momentum equations again with the updated pressure field, for correcting the velocity field. The species conservation equations along with the energy equation are solved using an explicit time marching scheme with a smaller time step value for a certain number of inner iterations. The thermo-physical properties which are functions of temperature are then updated. The reaction rates for the 17-step kinetic scheme are also calculated at the updated temperature and concentration values. This transient marching procedure is carried out until a time independent solution evolves. A certain number of iterations are carried out initially (for flow solution alone) without solving the energy and species transport equations. After obtaining the cold flow solution, a suitable high temperature region is patched near the jet inlet, so that ignition occurs followed by sustained combustion. The solution methodology outlined above has been implemented using a FORTRAN code and computations have been carried out on Intel Pentium III processor based Personal computers, SGI workstations and HP cluster machines. Typical run time for each simulation was of the order of 100 h on a non- uniform 181 × 121 grid, with a typical flow marching time step of 10^{-4} s and a kinetic time step of 10^{-6} s.

2.5. Grid independence study

In order to assess the sensitivity of the predicted solutions on the grid employed, grid independence studies have been carried out. Non-uniform grids with finer step sizes were placed near the burner exit in the z-direction and between 0 and $1.0d_j$ in the r-direction. The change in the dimensional maximum temperature (T_{max}) with respect to change in the grid structure was monitored to determine the grid independence of the predictions. The results of a typical case with $Re = 55$ are shown in Table 3. When the total number of grid points used for the computations was increased from 181 × 121 to 241 × 181, a change of only 0.114% with respect to the previous value of $T_{max}$was observed, even though the number of grid points was doubled. Hence, a 181 × 121 grid was employed for all the subsequent calculations.

3. Experimental procedure

A schematic of the experimental set up is shown in Fig. 2. The experiments have been conducted using an atmospheric pressure burner of 8.0 mm fuel tube diameter. Fuel is injected vertically into the fuel tube and co-flow air is sent through a concentric burner pipe of 99.0 mm inner diameter. The fuel and air flow rates are varied in the range 1.5–4.2 $cm^3\ s^{-1}$ and 58–630 $cm^3\ s^{-1}$, respectively (at ambient temperature). The air passage has been designed to ensure laminar and uniform velocity distribution (except for the boundary layer) at the burner exit, while the fuel passage yields fully developed laminar pipe flow. The fuel and airflow rates are measured using calibrated rotameters. Pressure regulators are used to monitor and provide a constant pressure gas supply across the rotameter. Experiments were conducted using industrial quality ethylene gas with a purity of 99.5% at different Reynolds numbers, viz. $Re = 28$, 42, 55 and 70. The luminous ethylene diffusion flames at different Reynolds numbers have been photographed using a digital camera and analyzed with the help of standard image-processing software such as Image J and IrfanView.

Experiments were also carried out with methane (99.5% purity) for a comparative assessment of the flames. The effect of co-flowing air velocity has been studied by varying the air flow rate for each fuel flow rate. Soot deposition rates (SDR) at different axial locations were obtained by the method of thermophoretic deposition on a stationary surface [26]. In this experiment, a proper fixture has been designed and attached to a traversing mechanism to hold the stainless steel plate in position for the deposition of soot. Soot was collected for a period of 25 s at different axial positions. The plate was covered with aluminum foil before and after deposition of soot to prevent moisture absorption.

Visible flame shapes were derived from the digital photographs by a method of edge detection, using image-processing software. This method involves averaging the

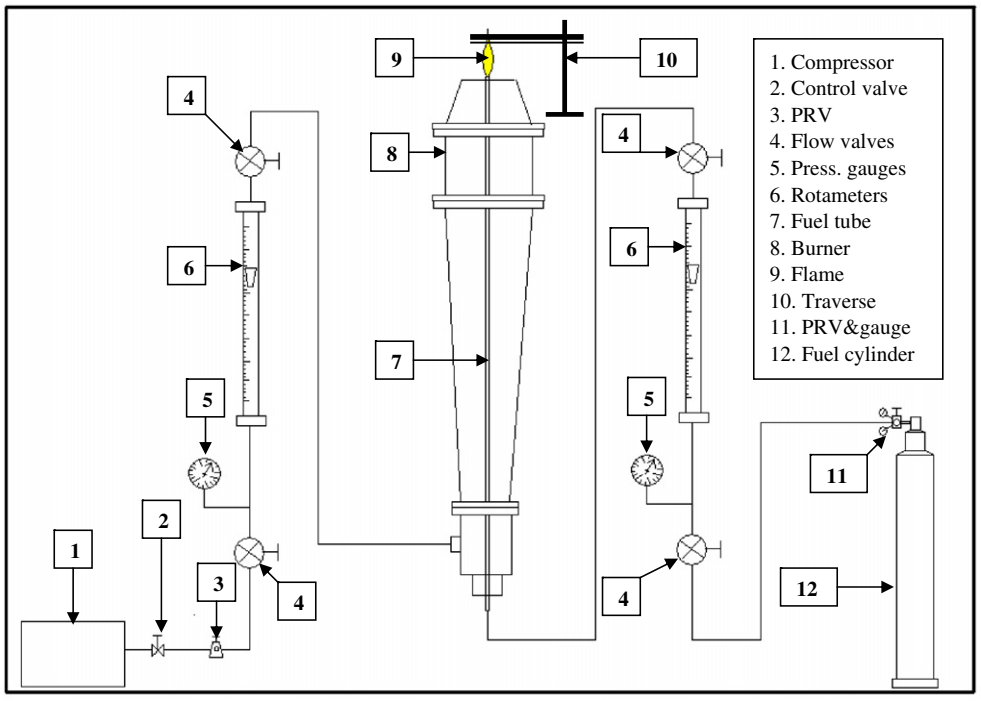

Fig. 2. Schematic of the experimental set up for studying jet diffusion flames.

frames of photographs extracted from a video of the laminar flame taken for a duration of 15 s. Averaging of the images is necessary to eliminate the uncertainties in the flame height measurement due to slight fluctuation or flickering of the flame. The flame boundary is identified by the edge detection operation, in-built in the software. Edge detection is straightforward in an ethylene diffusion flame, due to the existence of soot and associated luminosity.

The individual uncertainties in calculating the area of the fuel pipe and co-flow air nozzle are 0.23% and 0.28%, respectively. The uncertainty "u" of a quantity R, which is a function of several variables $x_1,\ldots,x_N$ can be found with good accuracy using a root-sum-square combination as

$$u_R = \left[\sum_{i=1}^{N}((\partial R/\partial x_i)u_i)^2\right]^{0.5}, \quad (26)$$

where, u_i is the uncertainty in the generic variable x_i.Uncertainties for the derived quantities are estimated using this relation. The uncertainty in mass flow rate measurement using the rotameter is 0.5%. Other quantities that contribute to the overall uncertainty in the final result are the flow velocity and Reynolds number, deposition rate of soot and the flame height. The uncertainty with velocity measurement and Reynolds number are estimated to be within ±0.81% and ±1.42%, respectively. Temperature measurements are carried out using a calibrated, uncoated R-type thermocouple with appropriate compensation for radiation heat loss [27]. The estimated uncertainty in temperature measurement is within ±40 K. The uncertainty in soot measurements is within ±1.8% and that of the flame height is within ±0.38%.

4. Results and discussion

Before embarking upon a detailed discussion of results from the present study, it was felt desirable to validate the present model predictions with results available in published literature ([14,15]). Using a 64-step detailed kinetic model, Kennedy et al. [14] simulated the case of ethylene combustion for the configuration experimentally investigated by Santoro et al. [15]. For the same problem, the present model with reduced 17-step chemistry provides predictions of similar accuracy as the detailed chemistry model [14]. After this validation exercise, a parametric study highlighting the effects of Reynolds number on the flame shape, temperature profile and soot distribution has also been presented, along with comparisons between the present experimental and numerical results.

4.1. Comparison with published data

Fig. 3 shows the temperature profile as a function of non-dimensional radius at an axial distance of 70 mm, for the ethylene diffusion flame corresponding to a fuel flow rate of 3.85 $cm^3\ s^{-1}$ through a fuel pipe of 11.1 mm diameter and co-flow of air at the rate of 713 $cm^3\ s^{-1}$, through a concentric annulus of 102 mm outer diameter. The detailed kinetic model results of [14] and the experimental data of [15] for this configuration are also plotted. Predictions for the cases with and without radiation heat transfer

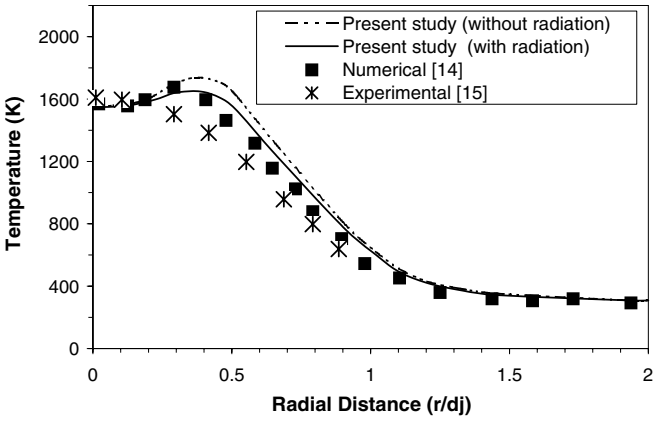

Fig. 3. Predicted and measured temperature profiles at $x = 70$ mm for the validation problem.

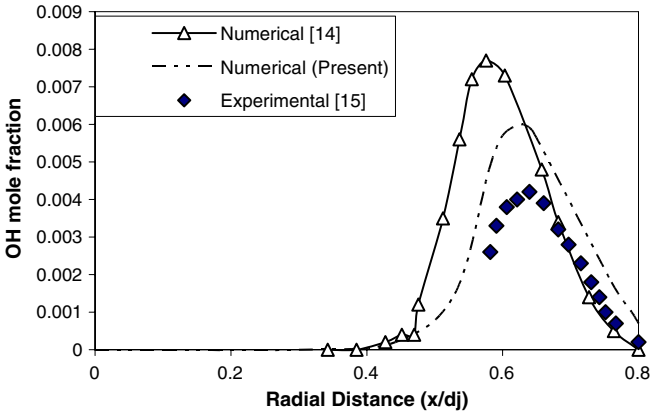

Fig. 5. Predicted and measured OH mole fractions at $x = 7$ mm for the validation problem.

using the present reduced chemistry model are shown for comparison. The general features of the radial temperature profile are reproduced quite well by the present model. However, the peak temperature value is observed to occur a little farther from the axis than in the simulations of Kennedy et al. [14]. Although such minor differences exist, in an overall sense, the present model performs quite well compared to the 64-step detailed kinetic model (in some cases, even better than the detailed model), especially when radiation heat transfer due to soot, carbon dioxide and water vapor is taken into account. The effect of radiation from the flame is to reduce the temperature, as shown in Fig. 3.

In general, all the three numerical models predict a higher peak temperature as compared to the experimental data of [15]. Kennedy et al. [14] have indicated some possible reasons for such deviations observed. In Figs. 4 and 5, the radial profiles of soot volume fraction and OH mole fraction predicted by the present model are plotted along with the corresponding results of [14,15]. In the cases compared, the reduced chemistry model fares better than the detailed chemistry model, closer to the axis of the flame.

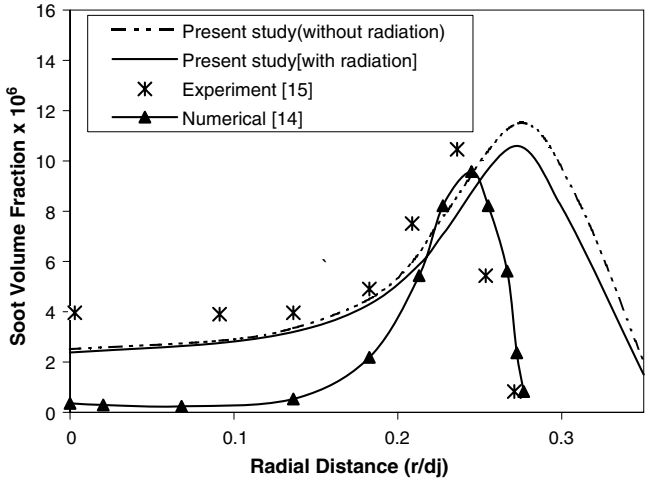

Fig. 4. Predicted and measured soot volume fractions at $x = 50$ mm for the validation problem.

At radial positions far away from the axis, the detailed chemistry model of Kennedy et al. [14] gives better predictions. The flame radius and reaction zone predicted by the present model are slightly wider. The slower oxidation of soot by OH observed in the predictions of the present model, results in a wider temperature profile in the radial direction, due to soot radiation. Given the fact that the chemical kinetics as well as the transport property models are very different between the earlier and the present work, the agreement seen in the results is fairly good.

4.2. Results of the parametric study

Numerical simulations and experimental measurements have been carried out using a fuel pipe of 8 mm inner diameter, resulting in the fuel jet Reynolds number range of 28–72. The flame shape, radial and axial temperature distributions, and the soot mass flux at different heights within the flame, have been measured and compared with the numerical predictions at different fuel jet Reynolds numbers. In the cases studied here, soot which is formed in the bottom part of the flame gets oxidized in the top part and eventually very little soot is present beyond the combustion zone. The terminology "non-sooting" was proposed by Santoro et al. [15] in order to distinguish such a diffusion flame that does not emit soot from the tip of flame; the present experiments mostly correspond to non-sooting flames, except for the case of $Re_j = 72$, when slight emission of soot was observed at the flame tip.

Photographs of luminous ethylene diffusion flames at different Reynolds numbers are shown in Fig. 6. Comparisons between the flame heights observed in experiments and numerical predictions are shown in Fig. 7, for the ethylene flame. Experimental results for methane combustion are also shown, to illustrate the effect of the fuel employed. The numerical predictions are in excellent agreement with the experimental observations. It is also evident that a linear relationship exists between the Reynolds number and flame height, for the laminar flow regime considered in the present study. The trends are also in good agreement

Fig. 6. Ethylene diffusion flame: (a) $Re = 28$, (b) $Re = 42$, and $Re = 55$.

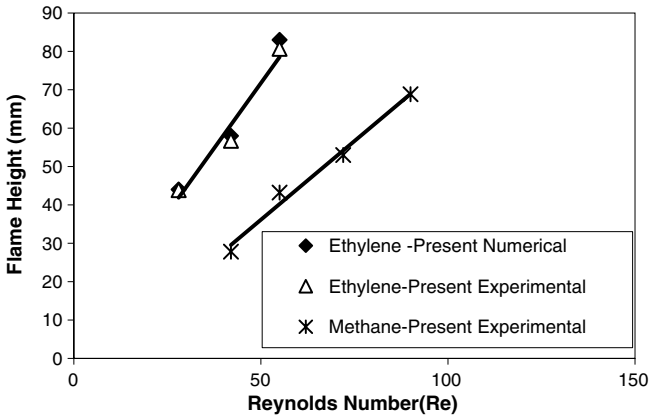

Fig. 7. Comparison of flame heights for various Reynolds numbers.

with the correlations proposed by Ropper et al. [4] for circular port burners. It has been observed that the ethylene flames are longer and more luminous compared to methane flames. The higher luminosity is due to the presence of soot in ethylene flames. The effect of co-flow was also studied by varying the air velocity (Fig. 8) as equal to 25%, 50%, 75% and 100% of the fuel jet velocity. No significant change in flame height was observed with the variation of co-flow air velocity. This independence with respect to co-flow air velocity can be attributed to the over-ventilation of the open diffusion flames under consideration. At the highest

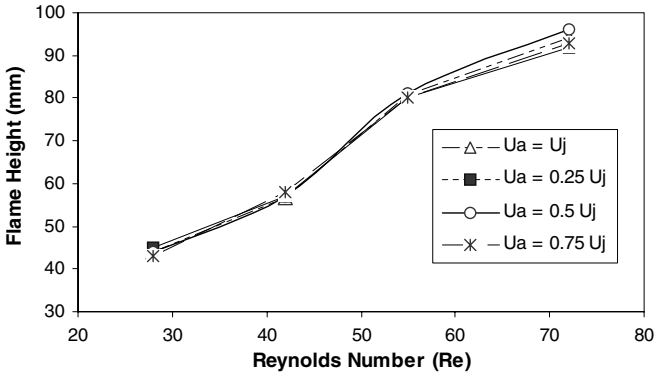

Fig. 8. Effect of co-flow air velocity on the flame height at different Reynolds numbers.

Reynolds number ($Re = 72$) considered in the present study, an accurate measurement of flame height was difficult, because of soot emission from the tip of the flame. Also, buoyancy effects become important for the taller flames. Hence, exact linearity of the flame height with respect to Reynolds number is not observed.

Fig. 9 shows the predicted radial variations of fuel and oxygen mass fractions at two different Reynolds numbers, for an axial location corresponding to half of the flame height. Here, the Reynolds number has been varied by changing the fuel flow rate. At a higher Reynolds number, as the flame becomes taller, the lateral spread for the fuel jet increases. Due to the greater lateral spread as well as the consumption of fuel in combustion reactions, the fuel mass fraction value is smaller near the axis for a higher Reynolds number whereas it is more at larger radial distances. The oxygen mass fraction distribution, as expected, displays trends that are opposite to that of fuel mass fraction. The radial profiles of soot volume fraction (Fig. 10) show that maximum soot fraction occurs away from the axis at half the flame height. Also, the location of maximum shifts further away from the axis with Reynolds number, due to the increase in size (both radial and axial) of the flame zone.

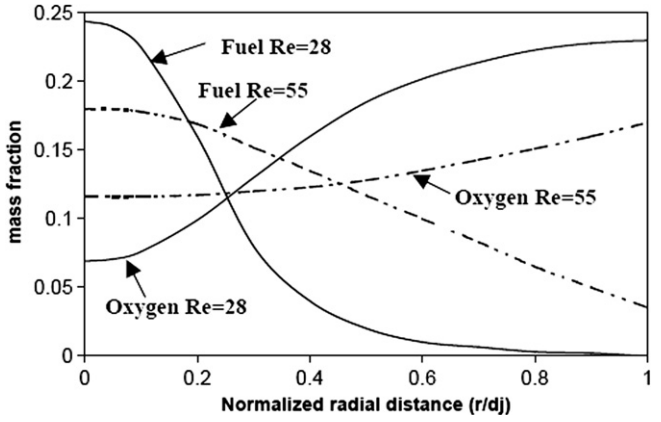

Fig. 9. Predicted radial variation of fuel and oxygen mass fractions at 50% flame height for different Reynolds numbers.

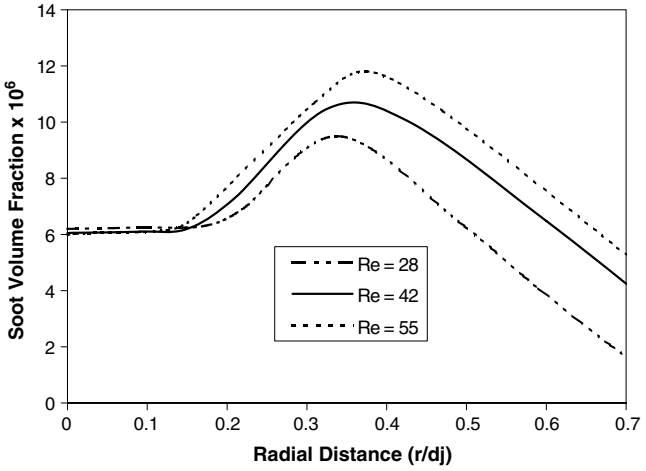

Fig. 10. Predicted radial variation of soot volume fraction at 50% of flame height for different Reynolds numbers.

The total soot deposition rates measured using the thermophoretic deposition technique are shown in Fig. 11, at different axial distances and Reynolds numbers. For the sake of clarity, the experimental data have also been fitted by curves that are shown as continuous and dotted lines in the figure. In all these cases presented, a complete burnout of soot is observed towards the tip of the flame. It is also clearly seen that in the bottom part of the flame, soot concentration increases (and hence collection rate also increases) due to the soot formation reactions. In the top part of the flame, soot decreases due to the oxidation steps. The height of the formation and depletion zones are not exactly equal – the oxidation region is relatively shorter than the formation zone for soot.

In any soot collection technique, the collection efficiency cannot be 100% and hence it is difficult to make an exact comparison between theory and experiment for the total soot flux. In order to avoid this difficulty, a plot of the dimensionless soot flux crossing an axial station (for theory) or the dimensionless soot flux collected at an axial location (in experiment) are plotted in Figs. 12a and 12b. The normalisation has been carried out using the maximum flux of soot crossing or collected in a particular flame as the scaling factor, for the results shown in these figures. For all the three cases, the positions of the peak soot flux are predicted well by the present model, as compared to the corresponding experimental results. However, the soot burnout at the tip of the flame occurs slightly earlier in the experiments than predicted by the simulations. This variation can be attributed to the heat loss from the flame to the plate inserted for the measurement of soot. The reduction in temperature results in enhanced OH production and early burnout of soot.

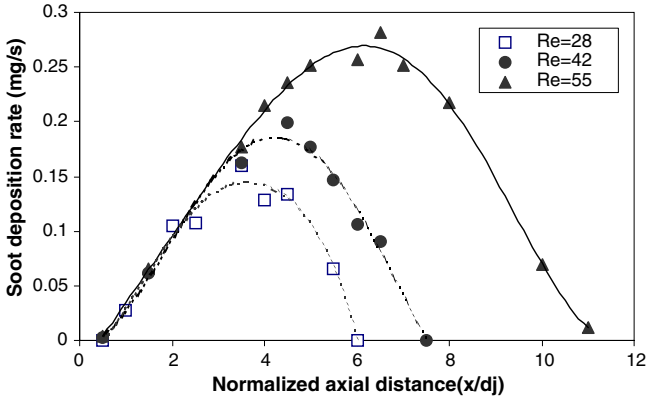

Fig. 11. Variation of total soot deposition rate (experimental) with axial distance at different Reynolds numbers.

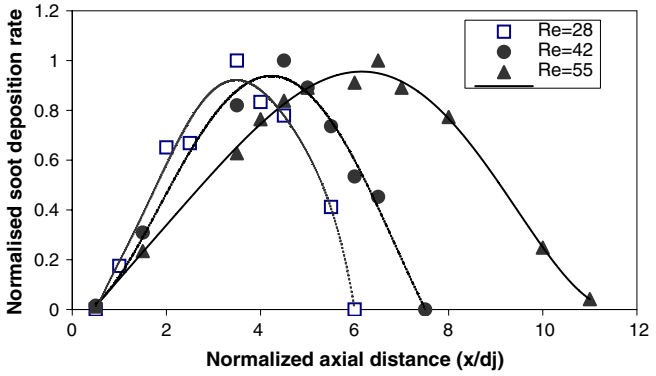

Fig. 12a. Variation of normalized total soot deposition rate (experimental) with axial distance at different Reynolds numbers.

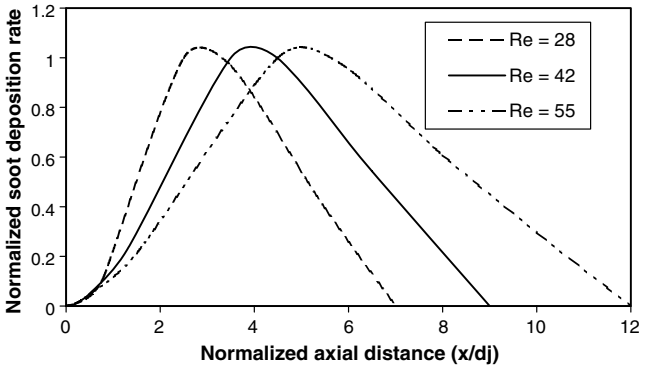

Fig. 12b. Predicted variation of normalized total soot deposition rate with axial distance at different Reynolds numbers.

The predicted mole fraction contours of CO_2, H_2O and soot are shown in Fig. 13a–c, respectively. The carbon dioxide and water vapour contours show maximum values within an axial distance of about 2–3 diameters, implying that the major combustion reactions occur in this zone. Kinetic steps for soot involving nucleation, surface growth, coagulation and finally oxidation, extend up to almost an axial distance of 12 diameters. The spreading out of carbon dioxide and water vapour contours at larger axial distances implies convective–diffusive transport of these species, while soot is completely oxidised at the tip of the visible flame (see Fig. 4).

Comparisons between the predicted temperature profiles and the corresponding experimental results for $Re = 55$ at

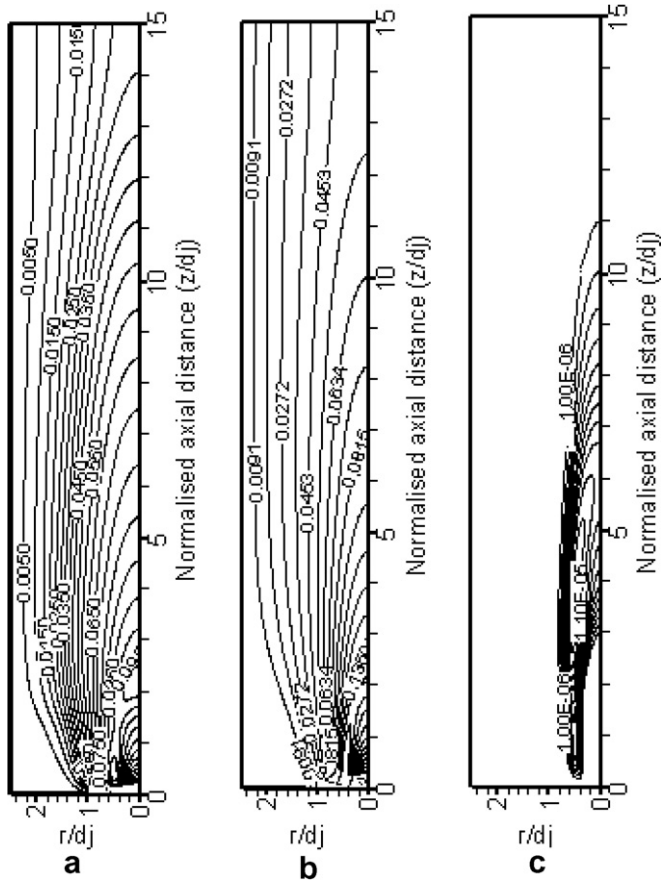

Fig. 13. Contour plots for $Re = 55$: (a) CO_2 mole fraction (b) H_2O mole fraction (c) soot volume fraction.

dimensionless axial distances (x/d_j) of 2.5 and 10, are shown in Figs. 14 and 15, respectively. The predictions have been carried out for the cases with and without radiative heat transfer. The numerical predictions show reasonable agreement with the experimental results for both the axial distances. An error of about 150 °C occurs in the peak temperature if radiation effects are ignored and the accuracy of the prediction improves after including the radiative heat transfer. Another interesting fact is that the location of the maximum deviation between the predictions of the model with radiation and that without radiation, coincide with the locations of maximum soot concentration, for both the axial sections. Thus, it is quite clear that soot plays an important role in distributing the heat generated by combustion through emission of radiation.

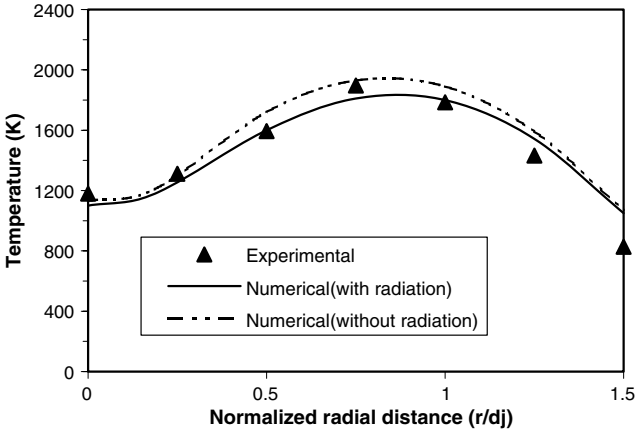

Fig. 14. Predicted and measured temperature profiles at $Re = 55$ for an axial distance of $x/d_j = 2.5$.

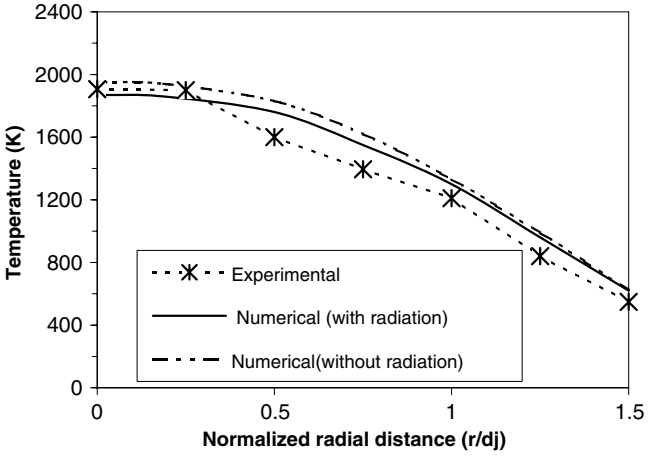

Fig. 15. Predicted and measured temperature profiles at $Re = 55$ for an axial distance of $x/d_j = 10$.

5. Conclusions

In this paper, axi-symmetric laminar ethylene–air diffusion flame has been numerically studied, with a reduced reaction kinetics involving sixteen species along with models for soot and radiation. Predictions of temperature, soot volume fraction and selected species are carried out and compared with earlier experimental as well as numerical results available in published literature. The results predicted with the present numerical model provide results that are at least as accurate as the predictions of the earlier detailed chemistry model, implying that if reduced chemistry steps are taken judiciously to represent all the important kinetic steps, it is possible to obtain fairly good predictions. Experiments and numerical simulations were also performed to study the effects of varying fuel and co-flow air velocities on ethylene diffusion flame characteristics. The results indicate that while major combustion reactions occur close to the burner mouth, the soot kinetics extend to a much larger distance. The inclusion of soot and radiation models improves the prediction of temperature and the peak temperature reduces by about 150 °C if radiative heat transfer is included. The flame size increases both axially and radially with fuel jet Reynolds number, and correspondingly the soot formation as well as oxidation zone sizes also increase. The velocity of co-flow air has very little effect on the combustion characteristics of the open diffusion flames studied here. The excellent comparison between the numerical and experimental results of the present study indicate that similar kinetic and transport models

can be employed for modeling the luminous diffusion flames occurring in many practical situations.

Appendix. Calculations of properties

As mentioned earlier in the text, thermo-physical properties have been evaluated using the Chapman–Enskog description of ideal gas mixtures [16]. The relations used for the evaluation of each of these properties are given below.

The density of the mixture is given by

$$\rho = \frac{p}{R_u T} M_{mix}, \tag{1}$$

where R_u is the universal gas constant and M_{mix} is the molar mass of the gaseous mixture at the particular location. For evaluating the specific heats of all the species, piecewise polynomials in temperature of the form $C_P = aT + bT^2 + cT^3 + dT^4 + eT^5$ have been used [21,28–30].

The viscosities and thermal conductivities for different species have been evaluated using the expressions

$$\mu = \frac{2.6693 \times 10^{-6}\sqrt{TM}}{\sigma^2 \Omega_\mu}, \tag{2}$$

$$k = \left(C_P + \frac{5}{4}\frac{R_u}{M}\right)\mu, \tag{3}$$

where σ is the hard sphere collision diameter [16] in Å and Ω_μ is a function of normalized temperature T^* (temperature scaled by ε/k). The quantities σ and ε/k are available in [16,21]. The binary mass diffusivity for a pair of species A and B is calculated by the empirical formula [16]

$$D_{AB} = \frac{0.0266\sqrt{T^3}}{P\sqrt{M_{AB}}\sigma_{AB}^2 \Omega_D}, \tag{4}$$

where $\sigma_{AB} = \frac{\sigma_A + \sigma_B}{2}$ and Ω_D is a function of T^*. Also, the mixture molecular weight is given by $M_{AB} = 2/(\frac{1}{M_A} + \frac{1}{M_B})$.

The mixture properties are evaluated using the ideal gas mixture formulation as

$$\rho = \sum_i \rho_i Y_i, \tag{5}$$

$$C_P = \sum_i C_{Pi} Y_i, \tag{6}$$

$$\mu_{mix} = \sum_{i=1}^{n} \frac{Y_i \mu_i}{\sum_{j=1}^{n} Y_j \phi_{ij}}, \tag{7}$$

$$k_{mix} = \sum_{i=1}^{n} \frac{Y_i k_i}{\sum_{j=1}^{n} Y_j \phi_{ij}}, \tag{8}$$

where the function ϕ_{ij} is given by [16]

$$\phi_{ij} = \frac{1}{\sqrt{8}}\left(1 + \frac{M_i}{M_j}\right)^{-\frac{1}{2}}\left[1 + \sqrt{\frac{\mu_i}{\mu_j}}\left(\frac{M_j}{M_i}\right)^{\frac{1}{4}}\right]^2. \tag{9}$$

References

[1] L.D. Savage, The enclosed laminar diffusion flame, Combust. Flame 6 (1962) 77.
[2] J.M. Jones, J.L.J. Rosenfeld, A model for sooting in diffusion flames, Combust. Flame 19 (3) (1972) 427–434.
[3] B. Leckner, Spectral and total emissivity of water vapor and carbon dioxide, Combust. Flame 19 (1972) 33–48.
[4] F.G. Ropper, The prediction of laminar jet diffusion flame sizes: part I and II, Combust. Flame 29 (1977) 219–234.
[5] R.E. Mitchel, A.F. Sarofim, L.A. Clomburg, Experimental and numerical investigation of confined laminar diffusion flames, Combust. Flame 37 (1980) 227–244.
[6] E.S. Oran, J.P. Boris, Detailed modeling of combustion systems, Prog. Energy Combust. Sci. 7 (1981) 1–72.
[7] M. Frenklach, H. Wang, M.J. Robinowitz, Detailed kinetics modeling of soot formation in shock-tube pyrolysis of acetylene, in: 20th International Symposium on Combustion, The Combustion Institute, Pittsburgh, 1984, pp. 887–901.
[8] N. Peters, R.J. Kee, The computation of stretched laminar methane–air diffusion flames using a reduced four-step mechanism, Combust. Flame 68 (1987) 17–29.
[9] K.M. Leung, R.P. Lindstedt, W.P. Jones, A simplified reaction mechanism for soot formation in nonpremixed flames, Combust. Flame 87 (1991) 289–305.
[10] M. Fairweather, W.P. Jones, R.P. Lindstedt, Predictions of radiative transfer from a turbulent reacting jet in a cross-win, Combust. Flame 89 (1992) 45–63.
[11] C.R. Kaplan, W.B. Seung, S.O. Elaine, L.E. Janet, Dynamics of a strongly radiating unsteady ethylene jet diffusion flame, Combust. Flame 96 (1994) 1–21.
[12] J.B. Moss, C.D. Stewart, K.J. Young, Modeling soot formation and burnout in a high temperature laminar diffusion flame burning under oxygen-enriched conditions, Combust. Flame 101 (1995) 491–500.
[13] H. Guo, L. Fengshan, J.S. Gregory, L.G. Ö Mer, A numerical investigation of thermal diffusion influence on soot formation in ethylene/air diffusion flames, Int. J. Comput. Fluid Dyn. 18 (2004) 139–151.
[14] I.M. Kennedy, Y. Clement, C.R. Darrel, R.J. Santoro, Modeling and measurements of soot and species in a laminar diffusion flame, Combust. Flame 107 (1996) 368–382.
[15] R.J. Santoro, H. Semerjian, R.A. Dobbins, Soot particle measurements in diffusion flames, Combust. Flame 51 (1983) 203–218.
[16] R.C. Reid, J.M. Prausnitz, T.K. Sherwood, The Properties of Gases and Liquids, third ed., McGraw-Hill Book Company, 1981.
[17] S.S. Sazhin, E.M. Sazhina, O. Faltsi-Saravelou, P. Wild, The P-1 model for thermal radiation transfer: advantages and limitations, Fuel 75 (1996) 289–294.
[18] M.F. Modest, Radiative Heat Transfer, Academic Press, New York, 2003.
[19] J.H. Kent, D.R. Honnery, A soot formation rate map for a laminar ethylene diffusion flame, Combust. Flame 79 (1990) 287–298.
[20] W.W. Yuen, C.L. Tien, A simple calculation scheme for the luminous flame emissivity, Fire Exp. Res. 6 (1967) 1481–1487.
[21] R. Turns, Stephan, An Introduction to Combustion: Concepts and Applications, International Edition., McGraw-Hill, Singapore, 2001.
[22] C.K. Westbrook, F.L. Dryer, Simplified reaction mechanisms for the oxidation of hydrocarbon fuels in flames, Combust. Flame 27 (1981) 31–43.
[23] L. Fengshan, H. Guo, J.S. Gregory, L.G. Ömer, Numerical modeling of soot formation and oxidation in laminar coflow non-smoking and smoking ethylene diffusion flames, Combust. Theory Model. 7 (2003) 301–315.
[24] D. Bradley, G. Dixon-Lewis, S.E. Habik, E.M. Mushi, The oxidation of graphite powder in flame reaction zones, in: Twentieth Symposium (Int.) on Combustion, The Combustion Institute, Pittsburgh, 1984, pp. 931–940.

[25] A. Garo, G. Prado, J.J. Lahaye, Chemical aspects of soot particles oxidation in a laminar methane–air diffusion flame, Combust. Flame 79 (1990) 226–233.
[26] E.G. Skolnik, E.T. Mc Hale, Sampling of soot in diffusion flames, Combust. Flame 37 (1980) 327–330.
[27] D. Bradley, K.J. Matthews, Measurement of high temperatures with fine wire thermocouples, J. Mech. Eng. Sci. 10 (1968) 299–305.
[28] C.H. Chiang, M.S. Raju, W.A. Sirigano, Numerical analysis of convecting, vaporizing fuel droplet with variable properties, Int. J. Heat Mass Transfer 35 (1992) 1307–1324.
[29] JANAF thermochemical tables, J. Phys. Chem. Ref Data 14(1) (1985).
[30] V. Raghavan, V. Babu, T. Sundararajan, R. Natarajan, Flame shapes and burning rates of spherical fuel particles in a mixed convective environment, Int. J. Heat Mass Transfer 38 (2005) 5354–5370.